JACS
JOURNAL OF THE AMERICAN CHEMICAL SOCIETY

Article

pubs.acs.org/JACS

Crystal Structures and Emission Properties of the BF_2 Complex 1-Phenyl-3-(3,5-dimethoxyphenyl)-propane-1,3-dione: Multiple Chromisms, Aggregation- or Crystallization-Induced Emission, and the Self-Assembly Effect

Petra Galer,[†] Romana C. Korošec, Maja Vidmar, and Boris Šket*

Faculty of Chemistry and Chemical Technology, University of Ljubljana, Aškerčeva 5, SI-1000 Ljubljana, Slovenia

Supporting Information

ABSTRACT: It is known that electron donating groups have quite a different effect on the π-delocalization of a conjugate system when bonded at ortho and para as compared to meta positions in the phenyl ring. In the present work, the BF_2 complex of 1-phenyl-3-(3,5-dimethoxyphenyl)-propane-1,3-dione (**1**), a molecule with two methoxy groups in one of the phenyl rings at meta positions, was prepared. Compound **1** exists as two polymorphs having different mutual orientations of the two methoxy groups: in polymorph A away from each other (termed anti), while in polymorph B one methoxy group is oriented toward the other (syn−anti). In both crystals, the molecules which are antiparallel (the subPh rings as well as dioxaborine are on opposite sides) form stacks through face-to-face $\pi-\pi$ interactions, while in polymorph A the crystal packing is further stabilized by intermolecular C(phenyl)−H···F and C(methoxy)−H···F hydrogen bonds. Solid A possesses numerous chromic effects, including mechano-, thermo-, and chronochromism, though the latter to a lesser extent, as well as the effect of rearrangement of the amorphous phase into a more stable crystalline phase A, associated with crystallization-induced emission enhancement (CIEE). The solid-state emission can be repeatedly switched regarding its color and efficiency with excellent reversibility by external stimuli. On the other hand, crystalline solid B undergoes thermal interconversion of syn−anti to the anti conformer. Compound **1** shows a solvatochromic effect (SE), is aggregation-induced emission (AIE) active, and through the sublimation process displays self-assembling crystalline platelike microstructures or microfibers that reveal an obvious optical waveguide effect.

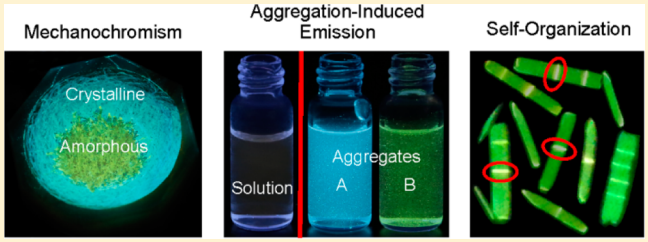

1. INTRODUCTION

Organoboron complexes form one of the important classes of fluorescent dyes.[1] Most dyes exhibiting fluorescence in dilute solution display quenched or reduced fluorescence intensity in the solid state.[2] However, some systems exhibit enhanced solid state emission[3] in which restriction of intramolecular rotation has been identified as the main reason for this effect.[4] Other intra- or intermolecular phenomena are involved as well, such as conformational changes, $\pi-\pi$ stacking, hydrogen bonding, and so forth, which cause rearrangements of the energy levels of emissive excited states.[5] In some cases, the crystalline phase proved to be a more efficient emitter than the amorphous phase,[6] showing the influence of molecular packing on the solid state emission. The effect is known as crystallization-induced emission enhancement (CIEE). A series of molecules that are nonemissive in the dissolved state are induced to emit efficiently when aggregated in the solid state; the effect is known as aggregation-induced emission (AIE).[1b,4,6,7] Various theories have been used to explain AIE phenomena, such as planarity and rotability, intramolecular restrictions, intermolecular interactions, aggregation caused quenching (ACQ) to AIE transformation, and so forth. AIE luminogens are therefore promising materials for utilization in optoelectronic and sensory systems as sensitive and selective chemosensors and bioprobes of the turn-on type.[8] Conventional fluorescent sensors commonly operate in a photoluminescence turn-off mode: an initially highly emissive dye becomes nonfluorescent when its molecules are induced to aggregate in the presence of a chemical species or biological analyte. In contrast, the unusual AIE effect has allowed the development of new type of sensing system that operates in a photoluminescence turn-on mode[9] by taking advantage of luminogen aggregation.

It is also known that in some cases the same fluorophores are present in the different polymorphs and consequently crystal-to-crystal interconversion with change in color emission can take place.[10] Mechanochromism[10b,11] is another phenomenon of color change resulting from mechanical grinding or pressing of a solid sample, and subsequent reversion to its original color through treatment such as heating or recrystallization. Fraser et al.[1d] published a communication describing the polymorphism and reversible mechanochromic luminescence (ML) of solid-state difluoroboron avobenzone (BF_2AVB). The morphology-sensitive solid-state emission of BF_2AVB was evident on

Received: February 25, 2014
Published: April 25, 2014

   dx.doi.org/10.1021/ja501977a | J. Am. Chem. Soc. 2014, 136, 7383−7394

mechanical perturbation. Single-crystal XRD revealed that BF_2AVB molecules can form multiple emissive aggregation states with different intermolecular interactions. Investigation of mechanical properties of green and cyan BF_2AVB crystals[12] using qualitative deformation tests and nanoindentation techniques confirmed that the cyan form is much softer and more compliant compared to the green one. ML experiments on green- and cyan-emitting polymorphs of BF_2AVB revealed that, upon smearing, the plastically deformable cyan form showed a prominent color change to yellow, while in the harder green form red-shifted emission was detected. On the basis of crystal structure analysis, the authors suggested that the presence of slip planes in cyan form is responsible for its higher plasticity compared to green form which has a nearly isotropic structure.

Commercially available avobenzone reacted with boron trichloride or tribromide to afford boron-bisavobenzone salts.[13] The complexes were found to exhibit unusual solvent-dependent fluorescence in solution and hydrochromic fluorescence in the solid state.

It was found later that various substituted difluoroboron dibenzoylmethane derivatives[1f,14] also exhibit ML in the solid state. In an article published recently,[1i] a mechanistic investigation of mechanochromic luminescent organoboron materials was carried out. By correlating solution data with solid-state results it was concluded that two coupled processes are responsible for the BF_2-dbm ML observed in the solid state: force-induced emissive H-aggregate formation and energy transfer to the emissive H-aggregates.

Development of luminescent materials is a hot topic of current interest because of its implications for the development of organic light-emitting diodes.[15] Molecular structures and conformations of dye molecules, as well as their morphological packing arrangements, affect their photophysical processes in the solid state. By preparing the BF_2 derivative, the β-diketone ring closure locked the conformation and blocked intramolecular rotations, making the crystals stronger emitters. Many boron-containing materials possess impressive optical properties.[16]

It should be mentioned that several substituted difluoroboron dibenzoylmethanes reported in the literature have a substituent bonded at the para position in one or both phenyl rings. However, it is known that electron donating groups have quite a different effect on π-delocalization of conjugate systems when bonded at ortho and para or at meta positions. It was found that the absorption and fluorescence spectra of the alkoxysilyl derivatives of dibenzoylmethanatoboron difluoride ($DBMBF_2$) depend on the position of the *O*-allyl or *O*-propyl alkoxysilyl substituent.[17] The highest fluorescence quantum yield is obtained from substitution at the para position, whereas that at the meta position gives the largest bathochromic shift in the fluorescence spectrum.

In the present article, we describe the BF_2 complex of 1-phenyl-3-(3,5-dimethoxyphenyl)-propane-1,3-dione,[18] a molecule with two methoxy groups in one of the phenyl rings at meta position. Different mutual orientations of the two methoxy groups in the crystal polymorphs result in two rotamers anti and syn−anti. Due to the small energy barrier between them, which is attributable to rotation of one of the methoxy group around the single C−O bond, interconversion of the rotamers by external stimuli can take place. Besides many other interesting photophysical properties, dye **1** exhibits especially rich chromic effects.

2. RESULTS AND DISCUSSION

Preparation of Polymorphs and Crystallography. Compound **1** was prepared from 1-phenyl-3-(3,5-dimethoxyphenyl)-propane-1,3-dione with $BF_3{\cdot}OEt_2$ in benzene.[18] The resulting yellow solid was filtered off (termed solid A, Figure 1b, entry (i), up). When dissolved in CH_3CN or CH_2Cl_2 and

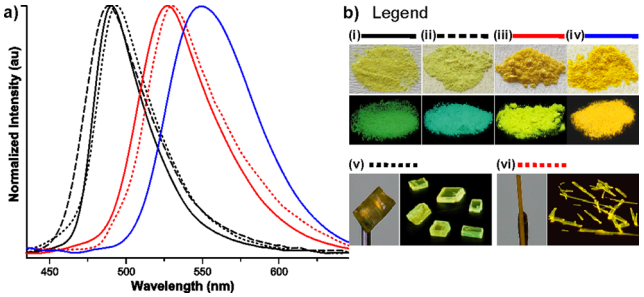

Figure 1. (a) Normalized fluorescence spectra of **1** in the solid state (λ_{ex} = 370 nm); solid A (black), solid B (red), solid C (blue). Solid, dotted, and dashed lines indicate pristine samples (as-synthesized), monocrystals and partially ground pristine solid A, respectively. (b) Legend together with photographs of the crystalline solids; (i), (ii), (iii), (iv) under UV lamp irradiation (below) and under ambient light (up) and monocrystals; (v) polymorph A, (vi) polymorph B under 365 nm UV lamp (right) and ambient light (left).

then the solvent evaporated, a solid with a different tint of yellow was obtained (termed solid B, Figure 1b, entry (iii), up).

Under UV black light excitation (λ_{ex} = 365 nm), solid A and solid B exhibited changeable color from green to turquoise blue and fluorescent yellow emissions, respectively; see Figure 1b, entries (i, ii, iii), below. To clarify the reason for the alteration of luminescence color and intensity of solids A (partially ground pristine solid A is a 1.3-times more efficient emitter, with a hypsochromic shift of 2 nm, than the pristine solid A), XRD analyses were carried out (Figure S1, Supporting Information (SI)). On the basis of the peak broadening in the diffraction pattern, the average size of crystallites of the pristine solid A and the corresponding partially ground crystals were estimated as 142 and 35 nm, respectively. These results confirmed our hypothesis about the dependence of the solid-state emitting properties upon the size of the crystals according to the observation of Mirochnik et al.[19]

On recrystallization from CH_2Cl_2/hexane, compound **1** formed two different types of crystals: greenish-yellow-emitting prismlike crystals (termed polymorph A, Figure 1b, entry (v), right) and yellow-emitting platelike crystals (termed polymorph B, Figure 1b, entry (vi), right). Simulated X-ray diffraction (XRD) curves showed distinctly different patterns for the two polymorphs. In comparison, XRD spectra of pristine samples of solids A and B totally coincided with the calculated diagrams of polymorphs A and B, respectively, proving the presence of only one phase (Figure 5, entry (i)). Also, the emission spectra of monocrystals A and B were nearly identical to those of the corresponding parent pristine solids, as shown in Figure 1a.

ORTEP drawings of polymorphs A and B (Figure 2) display the main difference in mutual orientation of the two methoxy groups; in polymorph A away from each other (termed anti) and in polymorph B the methoxy group bonded at C3″ position is oriented toward the other (called syn−anti). The polymorphs are triclinic and crystallize in the $P\bar{1}$ space group (additional crystal data, data collection, and refinement are

dx.doi.org/10.1021/ja501977a | J. Am. Chem. Soc. 2014, 136, 7383−7394

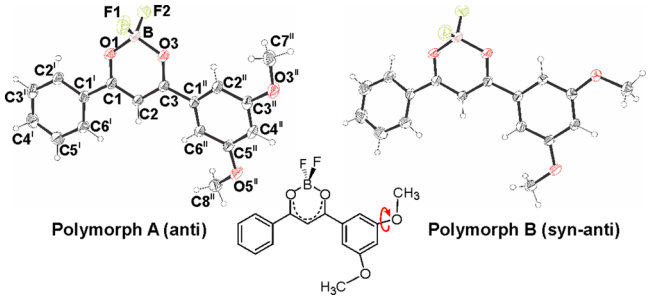

Figure 2. ORTEP drawings and atom labeling of the polymorphs.

summarized in Table S1, SI). In the crystals the molecules are not planar, both arene planes being out of the central diketonate plane (for the Ph and subPh rings by 6.03° and 15.53°, or 15.38° and 2.74°, for polymorphs A and B, respectively; see Table S2, SI). Selected geometric parameters of the polymorphs in comparison with the *p*-methoxy derivative are given in Table S3, SI.

In polymorph A (Figure 3, left), the molecules which are antiparallel (subPh rings as well as dioxaborine are on opposite

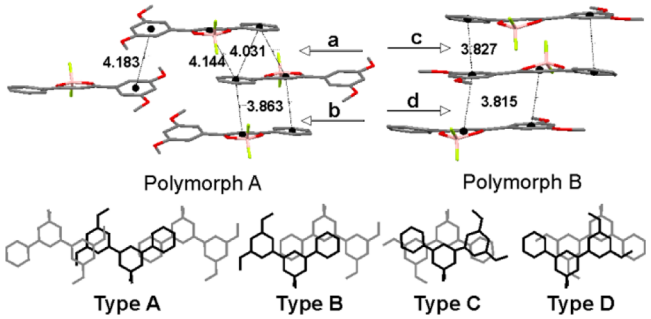

Figure 3. Partial view of the crystal packing through $\pi-\pi$ stacking interactions of polymorphs A and B with the given ring (C1′−6′; C1″−6″ and O1C1C2C3O3) centroid−centroid separations. The types of overlapping of the molecules are shown. Hydrogen atoms are omitted for the sake of clarity.

sides) form stacked trimers and dimers through face-to-face $\pi-\pi$ stacking interactions with two types of overlap arrangement. The first, type A (Figure 3) consists of both an arene−arene and a dioxaborine−arene pair stacked in such a way that the first molecule overlaps with either a subPh ring, or the Ph and dioxaborine rings of the two adjacent molecules. The total degree of overlap is 6% between parallel subPh rings and 20% of the surface area of the Ph ring at the ring centroid−centroid (Cg−Cg) distances of 4.183, 4.144, and 4.031 Å, respectively. The second, type B (Figure 3) includes the interactions between Ph and dioxaborine rings in the stacked dimer with a Cg−Cg separation of 3.863 Å; the degree of overlap of each pair is 13% of the Ph ring's surface area. The crystal packing is further stabilized by intermolecular interactions classified as C(phenyl)−H···F and C(methoxy)−H···F hydrogen bonds; see Figure S2, SI.

In polymorph B (Figure 3, right), the antiparallel molecules are packed in stacks with the arenes offset relative to each other forming two types of dimer. The Ph ring overlaps with the subPh ring and vice versa (type C overlapping) with 31% and 57% of overlap at the Cg−Cg distance of 3.827 Å, and type D where both dioxaborine rings are paired with subPh rings at a distance of 3.815 Å with 16% of the subPh ring area overlapping for each pair. Contrary to polymorph A, there are no remarkably strong intercontacts. The other differences in the molecular arrangement of the two polymorphs are mostly reflected in the $\pi-\pi$ stacking geometry. The higher degree of overlap results in stronger $\pi-\pi$ interactions which helps to explain the relatively large red-shift of F_{max} and the reduction of efficiency observed in the solid state emission of polymorph B versus polymorph A.

To provide a more effective understanding of the emission behavior of polymorphs A and B we employed DFT calculations in the gas phase with complete geometry optimization for the ground-state structures at the B3LYP/6-31G(d,p) level using the Spartan'14 software package for all four possible rotation isomers (Figure S3, SI): anti, syn−anti, anti−syn, syn, based on the mutual orientation of the methoxy groups in the substituted phenyl ring.

Figure 4 shows the highest occupied molecular orbital (HOMO) and the lowest unoccupied molecular orbital

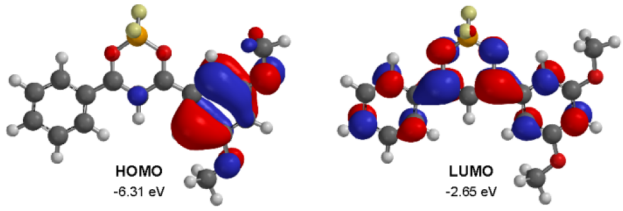

Figure 4. Molecular orbital diagrams for the HOMO and LUMO of the anti isomer of **1**.

(LUMO) of the anti isomer. The π-orbital of the entire structure lies on the LUMO, which is predominantly π^* in character, while the HOMO is localized on the whole of the substituted phenyl group. The oxygen atoms of both methoxy groups are involved in the HOMO but not in the LUMO. The relatively high energy level of the occupied orbitals of the subPh group prevents the HOMO from locating the π-orbital on the 1,3-diketone moiety. There is not much difference in the molecular orbital diagrams of the HOMO and LUMO for the anti isomer and the other possible structures syn−anti, anti−syn and syn. The energy levels of frontier molecular orbitals are given in the Supporting Information, Table S4.

In all cases, the unsubstituted phenyl ring deviates from the central diketonate planarity by practically the same angle of about 17°, except for the syn isomer, in which the angle is 13.2°, while the dihedral angles for the dimethoxy phenyl ring depend on the orientation of the methoxy groups (Table S5, SI). In addition, the anti orientation of the methoxy group in anti and anti−syn isomers toward the difluoroborine group is reflected in a lower energy (Table S4, SI). The higher stability of the anti−syn isomer in comparison with the anti one (ΔE = 3.21 kJ/mol) can be explained by the smaller dihedral angle between the plane through the subPh ring and the central diketonate moiety (12.1° and 15.0°, respectively). Rotation of the subPh ring around the C3−C1″ bond by 180° in the syn−anti isomer results in the anti−syn orientation lowering the energy by 5.51 kJ/mol.

Chromic Processes. Since the solid state emission properties strongly depend on the molecular structure and its packing in the crystal, alteration of molecular arrangements in response to heat, pressure, dropwise treatment[11e] with a solvent, and so forth are manifested as changes in emission color and intensity.

dx.doi.org/10.1021/ja501977a | J. Am. Chem. Soc. 2014, 136, 7383−7394

When pristine solid A with a fluorescence band centered at 490 nm (the spectrum is plotted in Figure 1a) was thoroughly ground in an agate mortar for 10 min, dramatic changes were observed in luminescence color and intensity with a drastic red-shift to 526 nm and a reduction of emission efficiency by as much as 5.3-fold. (J_0/J = 5.3 where J and J_0 are the emission efficiency obtained as the integrated area under the fluorescence peaks of thoroughly ground and pristine sample A, respectively.) The observed weak and red-shifted emission band can be attributed to the effect of a loose packing pattern in the amorphous solid. Additionally, mechanochromic emission changes in solid A were also investigated by powder X-ray diffraction (XRD) measurements. The XRD pattern of the unground sample showed intense and sharp reflection peaks, in good agreement with the simulated pattern of polymorph A (Figure 5, entry (i), solid A). After grinding, the XRD profile

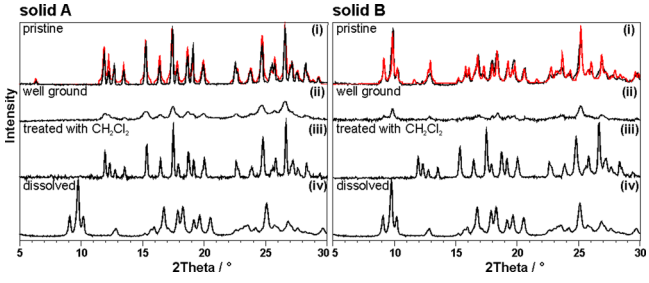

Figure 5. XRD pattern changes for powder sample of **1**, solid A (left) and solid B (right). The measurements were carried out in the order (i) pristine samples (black), with calculated XRD curves of polymorph A and polymorph B also shown for comparison (red), (ii) well ground samples after grinding for 10 min, (iii) after dropwise treatment with CH_2Cl_2, and last (iv) after dissolution and exposure to a vacuum.

showed only a few weak and significantly broadened signals, indicating a transition from a crystalline to an amorphous phase containing microcrystallites which might have been produced during the grinding process or by formation from a metastable amorphous phase, which partially recovered spontaneously at room temperature (Figure 5, entry (ii), solid A). However, this speculation was further more closely examined by differential scanning calorimetry (DSC), XRD, and fluorescence spectroscopy (FS) measurements, and the results reported in the subsection DSC Measurements. Next, after careful treatment of the well ground powder of solid A with drops of dichloromethane, the yellow emission gradually reverted back to the original blue-shifted color, as well the restoration of clear reflection peaks, which well fit those of the pristine solid A (Figure 5, entry (iii), solid A), demonstrating reversion from the amorphous to the crystalline phase. Consequently, the data indicates that the various emission colors observed upon grinding may be ascribed to the mechanochromic effect, whereas the changes in the fluorescence efficiency are associated with the crystallization-induced emission enhancement (CIEE) activity of solid A.

In comparison, pristine solid B emits rather weak fluorescent yellow light at 527 nm with an emission efficiency 8.4-fold lower than that of the pristine solid A (for the spectrum see Figure 1a). Although mechanical grinding of pristine solid B caused little change in its physical appearance, emission color, and intensity, the XRD pattern disappeared entirely when it was thoroughly ground and so confirmed a morphological transition from the crystalline to the amorphous phase; see Figure 5, entries (i, ii), solid B. Furthermore, upon dropwise treatment of the well ground solid B with dichloromethane, the amorphous phase rearranged into the more stable crystalline phase A (Figure 5, entry (iii), solid B) via a partial dissolution and recrystallization process, accompanied by an obvious blue-shifted band at 490 nm with a pronounced enhancement in fluorescence intensity. But when the resulting solid A (Figure 5, entry (iii)) was completely dissolved in CH_2Cl_2 with subsequent evaporation of the solvent under vacuum, a reversible transformation from crystalline sample A to B occurred, which is further supported by the XRD diagrams in Figure 5, entry (iv). In contrast, the transition from one crystalline phase to another was not achieved after dissolving pristine solid B in various solvents such as CH_2Cl_2 or CH_3CN followed by evaporation.

Because of the more pronounced chromic effects of solid sample A (owing to its better organizability or crystallinity) its morphology-sensitive solid-state emission was studied by fluorescence spectroscopy in greater detail after mechanical- or heat-induced perturbation. (Note all spectra were measured as soon as possible on solid samples freshly ground in an agate mortar.) When the pastel-yellow-emitting well ground powder of solid A (Figure 6, form 1) was briefly heated with a heat gun

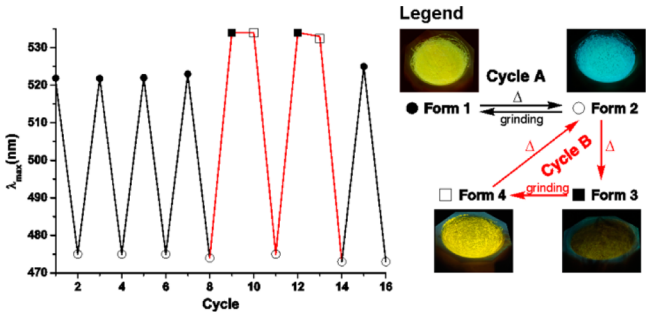

Figure 6. Reversible switching emission of solid A by repeated grinding–heating cycles: cycle A (black), cycle B (red), excitation wavelength = 370 nm. Photographs were taken in an agate mortar under UV illumination.

(~5–7 s), the resulting solid exhibited blue emission under UV blacklight excitation (λ_{ex} = 365 nm), (form 2). The corresponding emission maximum shifted from 523 to 474 nm, which closely matches the starting, unground solid emission, suggesting that the ground sample can revert back to the original crystal state, and indicating the repeatability of amorphization and crystallization by a grinding–heating cycle with almost no loss of emittance color and intensity (Figure 6, cycle A).

Next, when the blue-emitting solid obtained was further heated above the melting point, the color disappeared immediately and after just a few seconds at room temperature (rt), a virtually nonemissive, dark yellow solid emerged (form 3). To our surprise only a slight touch with the pestle changed its emission color to bright yellow; see Figure 6, form 4. The associated spectral band was significantly intensified with little fluctuation in its emission maxima ($F_{max} \approx$ 534 nm) in comparison to the initial state, form 3. The solid form 4, after intensive grinding followed by heating, could be converted back to the blue-emitting form 2 as shown in Figure 6, cycle B. Interestingly, besides being repeatedly switched in the solid state, its emissions could be reversibly tuned between the two

dx.doi.org/10.1021/ja501977a | J. Am. Chem. Soc. 2014, 136, 7383–7394

cycles (A and B) by the grinding−heating process, without exhibiting any degradation in luminescence.

DSC Measurements. To investigate the thermal properties and the structural changes after heating and grinding in more detail, DSC, XRD and fluorescence spectroscopy measurements of crystalline solids A and B were carried out. DSC measurements were performed in two heating and cooling cycles under an argon atmosphere. In the first cycle, the heating profile of solid A (Figure 7a) showed no peak up to the

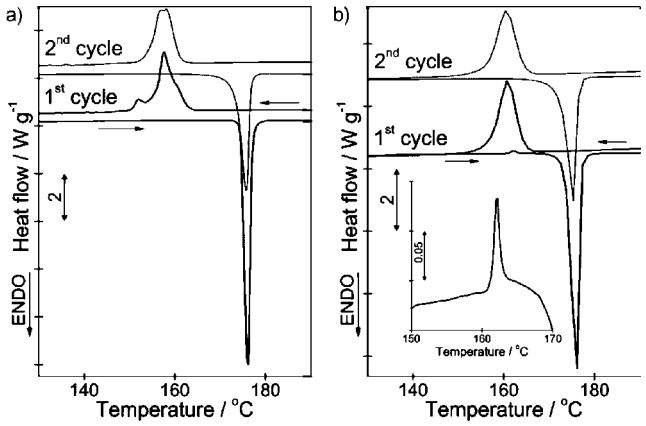

Figure 7. Two DSC heating and cooling cycles of (a) crystalline solid A and (b) crystalline solid B.

temperature of melting at 174.5 °C (ΔH_m = −100.1 J/g), indicated by the sharp endothermic signal. On cooling, an exothermic peak was observed at 161.7 °C (ΔH_s = 73.1 J/g) due to solidification of a new crystalline phase (termed solid C). The presence of this phase was proved by XRD; see Figure 8, entry (ii), and FS analyses. Thus, its emission spectrum

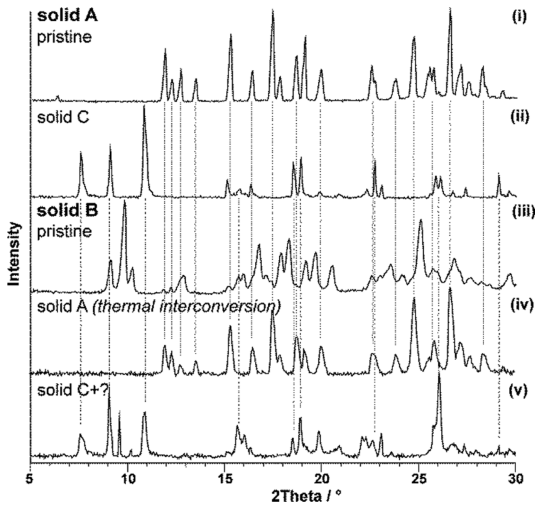

Figure 8. XRD pattern changes during annealing of crystalline solids A and B; (i, iii) pristine samples, (ii, v) after melting and cooling to rt, and (iv) after heating crystalline B to 162 °C and cooling to rt.

showed a substantial red-shifted band at 549 nm, accompanied by 14.5-fold weaker emission efficiency versus pristine solid A (Figure 1, entry (iv)). In contrast, the first heating cycle of crystalline solid B (Figure 7b) displayed a weak exothermic peak at 161.3 °C (ΔH = 0.6 J/g) before melting at 174.2 °C (ΔH_m = −93.4 J/g). The peak at 161.3 °C belongs to a phase-to-phase transition, suggesting that crystalline phase B converted to thermodynamically more stable crystalline phase A. An intermediate phase at 162 °C was carefully prepared by heating crystalline B to 162 °C directly in the DSC instrument. The XRD pattern of this intermediate phase confirmed phase transformation of crystalline solid B to crystalline A, since all the diffraction peaks were consistent with those of crystalline phase A; see Figure 8, entry (iv). On cooling, an exothermic peak was observed at 164.6 °C (ΔH_s = 67.7 J/g) due to solidification. The XRD pattern confirmed that besides phase C at least one additional crystalline phase was present (Figure 8, entry (v)). For this reason, the second heating and cooling cycles in both cases were slightly different. The melting point of a new pure phase C, obtained after solidification from the melt of crystalline A, was at 173.5 °C (ΔH_m = −74.5 J/g) and solidification at 161.2 °C (ΔH_s = 71.1 J/g); see Figure 7a. The mixture of phase C and additional phase(s) melted at 172.8 °C (ΔH_m = −70.3 J/g) and solidified at 164.6 °C (ΔH_s = 66.8 J/g); see Figure 7b.

To investigate further the stability of both polymorphs A and B, single point DFT calculations at the B3LYP/6-31G(d,p) level were carried out, using the geometries derived from the crystal structures. The data indicate that molecule A is 13.29 kJ/mol more stable than molecule B.

The DSC curves of amorphous solid A (amA) and B (amB), Figure 9a, which were obtained by intensive grinding in an

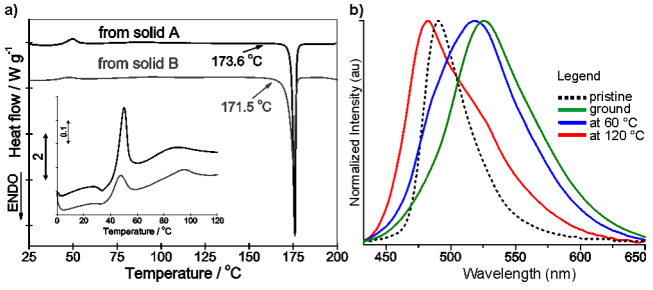

Figure 9. (a) DSC curves of amorphous solid A and amorphous solid B obtained after intense grinding of crystalline samples. (b) Normalized fluorescence spectra of amorphous A (green) and intermediate solids A, prepared after the first (blue) and the second (red) crystallization peak. The spectrum of pristine solid A (black, dotted line) is also shown for comparison.

agate mortar for 15 min, indicated that the yellow dye molecules of amA or amB undergo a glass transition at 32 °C,[14a] followed by two exothermic peaks due to crystallization in the temperature range from 35−60 °C and from 60−120 °C, respectively. The XRD patterns of the intermediate solids of amA or amB, prepared after the first (60 °C) and the second (120 °C) crystallization peak, confirmed the presence of crystalline solid A, even though their emission under UV light illumination was yellow and bluish green, respectively. The fluorescence spectra of amA and the intermediate solids are shown in Figure 9b. The average size of the crystallites obtained at 60 and 120 °C was calculated using the Scherrer equation as 31 and 54 nm, respectively. (The XRD patterns of the intermediate solids of amA are depicted in Figure S4, SI.) Closer inspection, however, reveals that the emission peak of thoroughly ground sample A progressively reverted back to the shorter wavelengths, quickly at 120 °C and slowly at room temperature. The time-dependent spontaneous recovery of the amorphous morphological structure back to the thermodynami-

dx.doi.org/10.1021/ja501977a | J. Am. Chem. Soc. 2014, 136, 7383−7394

cally stable crystalline state A, which is reflected in its changeable, blue-shifted emission band, is known as a chronochromic phenomenon.[20] In our case, photoluminescence restoration was stabilized after ~1.5 days under ambient conditions with a blue-shift of 8 nm, although it never recovered the identical spectral profile of pristine solid A, but could be switched back to the initial (red-shifted) emission wavelength by the grinding process. The data suggest that the ground sample A is in a metastable amorphous state and can crystallize promptly in the solid state on heating.

On further heating in the DSC instrument (after crystallization), a small difference in the melting temperature was observed for both investigated samples amA and amB of 173.6 °C (ΔH_m = −99.1 J/g) and 171.5 °C (ΔH_m = −90.7 J/g), respectively (Figure 9a). This temperature corresponds to the melting temperature of crystalline A (see Figure 7a).

Solid Films and the Self-Assembly Effect. While exploring morphology changes during thermal treatment of the crystalline solid B, we discovered another very interesting physical property—its appreciable vapor pressure. For this purpose, the DSC experiment was performed in such a way that a larger hole was made in the lid. An endothermic peak with an onset value at 160 °C was observed just before the phase transformation and melting, and a difference in sample weight occurred during the heating cycle (Δm = −17.2%) also confirming a low degree of sublimation, see Figure 11a. From this curve we established the sublimation temperature and applied this property of the compound for preparation of thin solid films. Sublimation is the key process responsible for production of self-assembling microstructures.

Next, the pristine solid B was gently smeared on a glass substrate and slowly heated to 162 °C in a hot stage microscope. The solid film microstructures before and after thermal treatment were examined by scanning electron microscopy (SEM) and confocal fluorescence microscopy (CFM).

From SEM, we clearly observed that the starting platelike crystals transformed to prismlike ones (Figure 10, entries (i, ii))

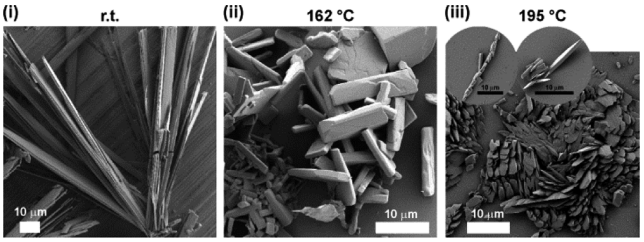

Figure 10. SEM images of morphology changes during thermal treatment of crystalline solid B.

and notably, from CFM a change in fluorescence spectra occurred from 528 to 481 nm as shown in Figure 11b, black- and red-dotted lines. Both mentioned methods were used to redetermine the heat-induced interconversion between the two crystalline phases. When heating was continued above the melting point to 195 °C, after cooling crystalline particles like scales were formed with a significantly red-shifted emission peak at 554 nm. The particle morphology is displayed in Figure 10, entry (iii), and the fluorescence spectrum in Figure 11b, blue dotted curve.

Next, we attempted to create a more stable amorphous film of **1** on a glass slide by spin-coating from dilute CH_2Cl_2

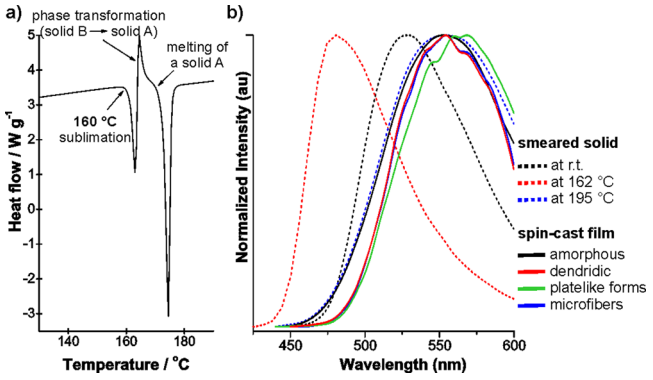

Figure 11. (a) DSC heating curve of crystalline sample B. (b) Normalized fluorescence emission spectra of the gently smeared crystalline solid B (black, dotted line) and the spin-cast film of **1** (black, solid line) in response to thermal stimuli monitored by CFM.

solution at 4500 rpm. The resulting solid film was naturally dried on standing at room temperature under an air atmosphere in the dark for a few days, before further investigation was done. Our success in obtaining a pure amorphous solid was supported by XRD, SEM, and CFM. The solid film (for the CFM microphotograph and corresponding XRD curve see Figure S5a, SI) exhibited a broad remarkably red-shifted emission band at 553 nm comparable to those of the pristine solid samples (Figure 11b, black solid curve). To our surprise, a small mechanical stimulus to the amorphous film, such as a slight touch with a spatula, formed some crystalline regions even before heating, as revealed by SEM analysis, suggesting a strong tendency of the amorphous form toward ordering; see Figure 12, entries (i, ii). A little thicker layer of the solid film obtained by spin-coating showed lower stability, converting spontaneously at room temperature to a more orderly state, namely a dendrite-like textured solid, within

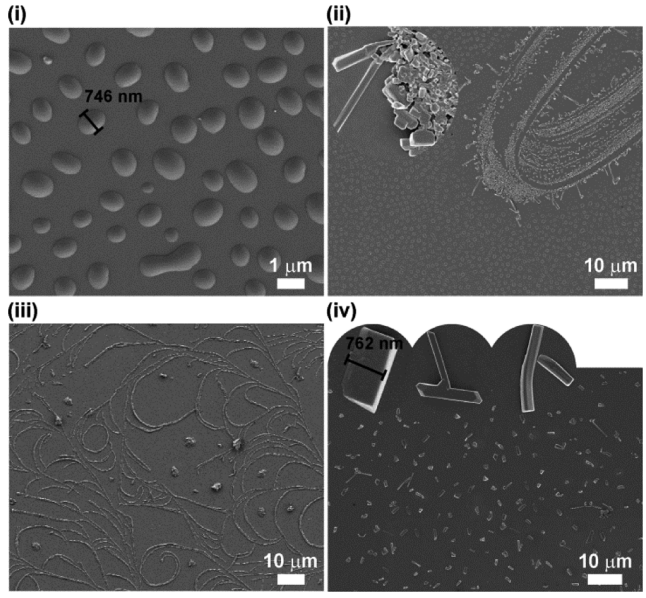

Figure 12. SEM images of (i) the amorphous phase obtained by spin-coating, (ii) mechanical pressure on the amorphous film with a spatula, (iii) dendrites obtained by heating the amorphous film to 120 °C, and (iv) crystallization of the amorphous form by heating for a minute at 162 °C.

dx.doi.org/10.1021/ja501977a | J. Am. Chem. Soc. 2014, 136, 7383−7394

1 h (Figure S5b, SI). Its emission band was nearly identical to that of the pure amorphous solid being red-shifted to 555 nm (Figure 11b, red solid line). Furthermore, when the pure thin amorphous film (Figure 12, entry (i)) was heated to 120 °C, a dendritic-like solid was also formed (Figure 12, entry (iii)). After careful thermal annealing at 162 °C for a relatively short time (because of its tendency to sublimation), the amorphous film crystallized in the more stable crystal state A, as depicted in Figure 12, entry (iv). Besides particle morphology, the figure also clearly displays the particle size, which is comparable with that of the amorphous form; see entry (i).

In order to evaluate the morphological structures and optical properties of the sublimate, an experiment was performed in which a second glass plate was placed a few millimeters above the amorphous film. Sublimation was carried out in two different ways. In the first case, the spin-cast amorphous film was heated at 160 °C until the sample had mostly sublimed, followed by cooling the cover glass bearing the sublimate to room temperature. The CFM image (Figure 13, entry (i))

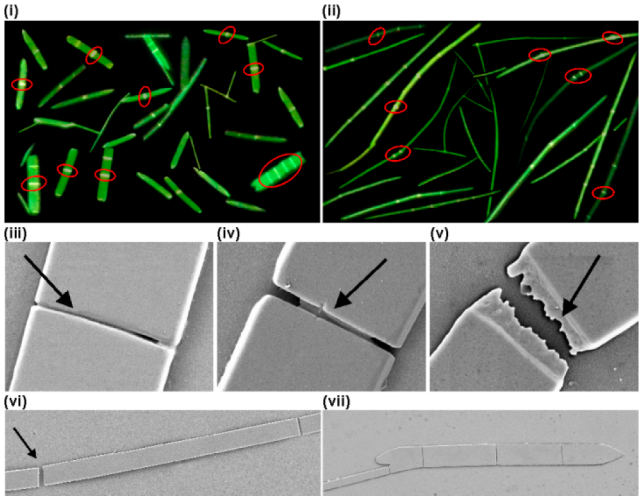

Figure 13. CFM images of fluorescent (i) platelike or needlelike and (ii) microfiber structures of the sublimate. Fluorescent images were taken under a fluorescence microscope with 405 nm excitation. SEM microphotographs of the self-organized structures show different levels of connection: (iii) fully filled with material connecting two crystals at the interface, (iv) partially filled, (v) separated segments containing residual material connecting two crystals at the interface, (vi) divided into invidual units, and last (vii) whole pointed-platelike structures.

shows that fluorescent structures with F_{max} = 564 nm were formed (the spectrum is plotted in Figure 11b, green solid line). A scanning electron microscope was also used to examine the morphology of the resulting solid (Figure S6a, SI). The results suggest that the platelike structures are built from segments (see Figure 13), which can be classified into three different levels of connection: the first, fully filled with material connecting two crystals at the interface (iii), the second, partially filled (iv), and the third, empty (vi) (see Figure 13). The terminal segment is typically pointed (vii). We believe that initially the segments were joined together by material connecting two crystals at the interface (probably of amorphous material), and that after some period of time they separated (v) and the material connecting two crystals at the interface disappeared (vi). In the second experiment, the amorphous film was rapidly heated to 210 °C so that sublimation occurred immediately and was then left at ambient conditions for a week. The resulting sublimate was analyzed by CFM and SEM. Evidently, a quite different sort of organized structure was formed. As seen from the SEM (Figure S6b, SI) and CFM microphotographs (Figure 13, entry (ii)), extremely thin (up to 1 μm) fluorescent crystalline microfibers with lengths of approximately several hundreds of micrometers, divided into segments, were formed. Upon excitation, these crystalline fibers emit green light of 555 nm (the fluorescence spectrum is shown in Figure 11b, blue solid curve).

To sum up, compound **1** is capable of self-assembly whereby its molecules pack one-dimensionally to give crystalline microstructures. Careful study by SEM and CFM revealed that the dazzling light emission which is seen along the microstructures (highlighted by the red circles in Figure 13, entries (i, ii)), indicates an obvious optical waveguide effect, operating in the light transmission process of the microparticles, as previously noticed and described by Tang and coworkers.[4e,20] On the basis of the SEM and CFM images (see Figure S7, SI), we assume that even the microstructures in phase A (F_{max} = 475 nm), crystallized from the spin-cast amorphous film, possess the waveguide effect.

Many larger, thicker microfibers, which can be observed even with the naked eye, up to 1 mm in length, were formed when an ethanolic solution of solid B was slowly evaporated on standing at room temperature (an optical image of the fibers is shown in Figure S6c, SI).

Solvatochromism. The optical properties of dye **1** were investigated in solution where free rotation around single bonds exists. Such motion around the C−O bond of the methoxy group causes equalization of the two polymorphs. The absorption and emission spectra of solid A and solid B in CH_3CN solution were identical, and both samples also gave identical ^1H and ^{13}C NMR spectra. However, the molecules of **1** in solution are characterized by the existence of a set of rotational states, which decreases the probability of the occurrence of a planar conformation and hinders overlapping of the molecules typical of the crystal state.

The effects of several solvents of various polarities on the electronic absorption and fluorescence spectra were examined. It is known that the surrounding medium (solvent) can effect a change in position, intensity and shape of the absorption or emission bands, an effect known as solvatochromism.[1a,b,21] In general, dye molecules with a large change in their permanent dipole moment on excitation exhibit strong solvatochromism. We found that the absorption spectrum of **1** was only slightly altered (in the range of 361−371 nm) with increasing solvent polarity (Figure 14). This observation implies that the ground-state electron distribution is not much affected, possibly due to lower polarity in the ground state than in the excited state.

In the emission spectra on irradiation at the charge transfer (CT) band (370 nm), compound **1** emitted from 431 nm in hexane (nonpolar solvent) to 534 nm in CH_3CN (polar solvent). The fluorescence emission peak underwent a red-shift with increasing polarity of the solvent, confirming a $\pi-\pi^*$ transition (Figure 14). According to the theory of solvatochromism greater differences between λ_{max} and F_{max} in more polar solvents indicate that the CT character in the first electronically excited singlet state is more polarized than that in the ground state. The difference between the ground- and excited-state dipole moments ($\Delta\mu$) of the solute molecule **1** was then determined from the Lippert−Mataga, Bakhshiev, Kawski−Chamma−Viallet, and Reichardt equations[22] based on a linear correlation between the wavenumbers of the ultra-

dx.doi.org/10.1021/ja501977a | J. Am. Chem. Soc. 2014, 136, 7383−7394

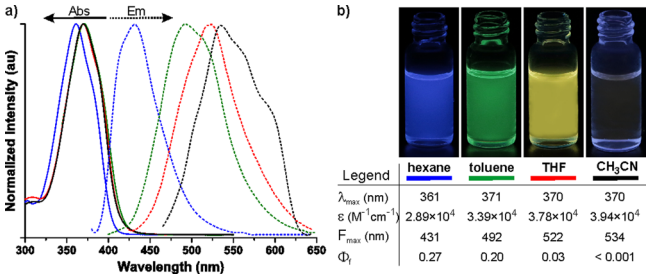

Figure 14. (a) Absorption (solid lines) and emission (excited at 370 nm, dotted lines) spectra of dye **1** in various solvents. (b) Optical properties of solutions of dye **1**: absorption (λ_{max}) and fluorescence (F_{max}) maxima, extinction coefficients (ε), and relative fluorescence quantum yield (Φ_f), estimated using quinine sulfate in 0.05 M H_2SO_4 as a standard. The photos of dye **1** in hexane, toluene, tetrahydrofuran (THF), and acetonitrile were taken under illumination with a UV lamp (365 nm).

violet–visible absorption and fluorescence maxima, and the bulk solvent polarity function, which involves both the dielectric constant and refractive index of the medium, or the molecular-microscopic solvent polarity parameter in the case of the Reichardt equation (see page S10 of the SI). All parameters necessary for determination of $\Delta\mu$ in the ground and excited states are collected in Tables S6–8, SI. The aforementioned methods suggest that the dipole moment in the excited singlet state (μ_e) is greater than the corresponding ground-state value (μ_g). This demonstrates a substantial redistribution of the π-electron densities between the two electronic states, leading to more polar species in the photoexcited state which is considerably affected by stabilization from the polar solvent as a consequence of stronger solvent–solute interactions in the excited state. It is worth noting from Table 1 that the discrepancies in the estimated values of $\Delta\mu$ observed may be due to approximations made in the different theories.

Table 1. Ground- and Excited-State Dipole Moments of 1 as Calculated by Various Methods

ground-state dipole moment, μ_g [a]			
vacuum	toluene	CH_3CN	
6.5 D	7.6 D	8.9 D	
difference between the ground- and excited-state dipole moment, $\Delta\mu$			
16.2 D[b]	9.7 D[c]	12.0 D[d]	7.8 D[e]

[a]Theoretical values of the anti isomer with complete geometry optimization obtained by employing the Spartan'08 suite of quantum chemical programs. [b]Value calculated from the Lippert–Mataga model. [c]Value calculated from the Bakhshiev model. [d]Value calculated from the Kawski–Chamma–Viallet model. [e]Value calculated from the Reichardt model.

Theoretical μ_g values in vacuum and in two solvents (being lower in less polar toluene than in acetonitrile) were evaluated by quantum chemical calculations using the DFT method adopting B3LYP/6-31G(d) level of theory; see Table 1. The Onsager cavity radius of solute molecule **1** (a = 6.2 Å) was determined by Kirillova's equation[23] using the static alpha polarizability parameter (α = 66.55 Å^3) from the computed wavefunction.

Interestingly, the fluorescence quantum yield Φ_f is also greatly dependent on the solvent polarity; thus, in hexane, it is approximately 300-fold higher that than in CH_3CN (Figure 14 b).

AIE Phenomena. The light emission of **1** induced by aggregate formation was also studied; in other words, the AIE activity of **1** was investigated.

A stock solution of **1** in CH_3CN (5×10^{-4} M) was prepared and an aliquot (1 mL) of this solution transferred to a 25 mL volumetric flask. After addition of a calculated volume of pure solvent, water (a nonsolvent of **1**) was added in two different ways: (a) in the first case, dropwise under vigorous stirring to give final 5×10^{-5} M CH_3CN–H_2O mixtures with different final water fractions (f_w = 0–90 vol %); (b) in the second case, a calculated quantity of water was added at once to prepare mixtures with water contents in the range of 0–99 vol % and the same final concentration. (Note that the suspensions with 95 and 99 vol % of water were derived from the recalculated initial acetonitrile concentration).

Dye **1** was virtually nonluminescent when dissolved in acetonitrile, as indicated by the negligibly small value of Φ_f and the photograph in Figure 14b. In fact, CH_3CN–H_2O mixtures with water contents up to 70 vol % were also practically nonemissive. A closer check of their fluorescence spectra revealed significantly broad and weak signals at $F_{max} \approx 556$ nm with small blue-shifts versus the spectrum of **1** measured in pure acetonitrile solution, as can be seen from the spectra shown in the inset of Figure S8a in the SI. When f_w = 10 was further increased up to 70 vol %, the emission intensity decreased to reach a straight line in the 70 vol % aqueous mixture. Moreover, both mixtures (prepared in different ways) up to 70 vol % of added water were observed to give identical spectral profiles. However, when a larger amount of water (f_w > 70 vol %) was added to the solution, the emission of dye **1** was turned on, as shown by the plot in Figure 15 on the right,

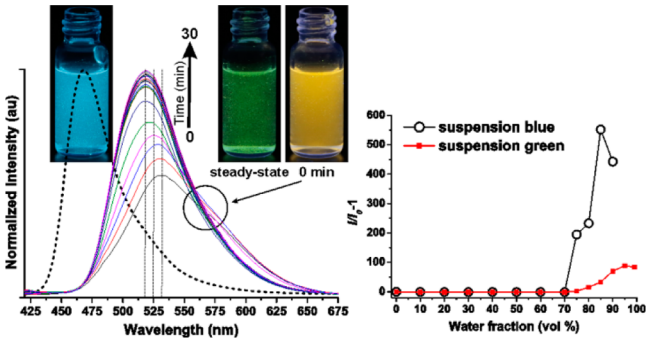

Figure 15. (Left) Emission spectrum of blue suspension of **1** (dotted line) and time-resolved emission spectra of green suspension (solid lines) in 5×10^{-5} M CH_3CN/water mixture at 85% and 95% fraction of water (f_w), respectively. Inset: photographs of suspension taken under UV lamp irradiation. (Right) Plot of $(I/I_0 - 1)$ values versus composition of the aqueous mixtures. I_0 = emission intensity in pure 5×10^{-5} M CH_3CN solution. Exciting wavelength: 370 nm.

caused by the formation of luminogen aggregates in aqueous mixtures with a high water content due to the insolubility of **1** in polar media such as water. The AIE activity of **1** is probably associated with its molecular structure, particularly with freely rotatable moieties in the molecule, which in dilute solution can undergo an active intramolecular rotation process, while in the aggregates this process is restricted, so the nonradiative relaxation pathway is blocked, thus making compound **1** a strong emitter.

dx.doi.org/10.1021/ja501977a | J. Am. Chem. Soc. 2014, 136, 7383–7394

The 75% aqueous mixture, prepared in the first way, emits significantly blue-shifted light at 469 nm with a drastic increase of its emission intensity (I/I_0 = 196) which is reflected in the rather narrow emission band (Figure S8a, SI). With increase in f_w, its emission was greatly enhanced and later (f_w = 85 vol %) reached its maximum efficiency value (I/I_0 = 553); see Figure 15. When the crystals or assemblies grow to critical sizes, precipitation occurs. This explains why the fluorescence emission did not increase further despite a further increase in the water fraction up to 90 vol %.

In the second way, the emission spectra of **1** remained practically unchanged from 10 up to 70 vol % of added water, as described previously in the first case. When the water fraction was increased to 75% the yellow emission was switched on (see Figure 15 on the right-hand side). Furthermore, very prompt reversion (occurring within a few minutes) from the initial yellow- to a green-emitting suspension was observed for different proportions of added water varying from 75 to 99 vol % (Figure 15, left). The intensity of the green emission increased with increasing amount of water, reaching a maximum at a 95% aqueous mixture (Figure S8b, SI). Aggregation as well as diverse color emission was followed by time-dependent fluorescence spectroscopy. For instance, after reaching a 95% aqueous mixture, a broad overlapping signal between 470 and 650 nm, centered at 532 nm appeared. In the stationary state, with time the emission band slightly intensified, becoming narrower and blue-shifted to 518 nm; see spectra in Figure 15. (Note: since the photoluminescence spectrum changed with time, all spectra were taken immediately after the samples were prepared.)

To further test our speculation on the origin of the three different emission colors of varying efficiency, we prepared experiments on a larger scale at 85% of water in order to isolate both aggregates by filtration of the resulting steady-state suspension. XRD analysis of the particles obtained from the blue-emitting suspension showed a totally identical pattern to that of solid A, while the pattern of the green suspension's aggregates was in accordance with that of solid B (Figure 16b).

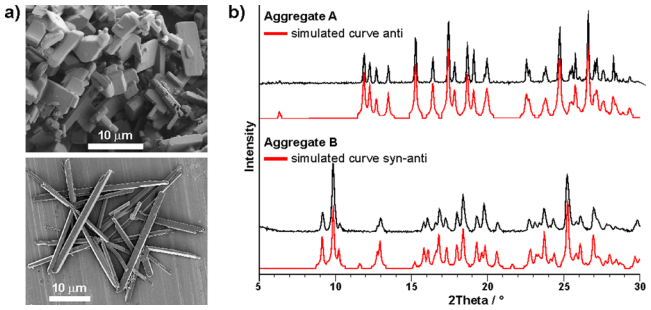

Figure 16. (a) SEM images of aggregate A (top) and B (bottom). (b) XRD diagrams: measured patterns of the aggregates are in black and the simulated one is in red.

This was supported by the SEM images that revealed well-defined prismlike and rectangular platelike aggregates A and B, respectively (Figure 16a). However, it is noteworthy that the fluorescence spectrum of the pure amorphous film well overlapped with that of the yellow suspension, suggesting that the crystallization or organization process favored the formation of crystals of solid B occurring through the first step, the so-called metastable amorphous state, as suggested by the photographs and time-dependent emission plot vs wavelength in Figure 15, indicated by the circle. Thus, the three distinct emission colors of **1** in suspensions with the same water content (f_w = 85 vol %) may be attributed to the different conformations and packing modes of the dye molecules in the aggregates.

To the best of our knowledge, this is the first time that the way of adding water and not its content in the mixture was utilized to fine-tune molecular packing during the aggregation process, allowing control of the selective production one of the desired solids. Evidently, a simple manipulation of the composition of the mixture or a small variation in the assembly environment can lead to a large change in the emission color and fluorescence efficiency of **1**. If water was added carefully (drop by drop), molecules of **1** at f_w > 70 vol % may cluster together slowly in an ordered fashion to form more emissive blue crystalline aggregates. When the water fraction becomes high in one step (as is described in the second case), the molecules may agglomerate quickly in a random way to form less emissive yellow amorphous particles, which are then converted over a short period of time into aggregates of the crystalline phase B.

3. EXPERIMENTAL SECTION

Structural and other crystallographic data (listed in Table S1, SI) have been deposited with the Cambridge Crystallographic Data Centre as supplementary publication number CCDC 988545 (Polymorph A) and 988546 (Polymorph B). A copy of the data can be obtained, free of charge, on application to CCDC, 12 Union Road, Cambridge, CB2 1EZ, UK fax: +44(0)-1223−336033 or by e-mail: deposit@ccdc.cam.ac.uk.

The $\pi-\pi$ stacking interaction was described by the degree of overlap in terms of the area shared by the rings, which was calculated in the following procedures: (a) project the area covered by subPh or dioxaborine rings on the arene ring in stacked pair; (b) calculate the intersection of the projected area of the ring and the area of arene ring; (c) take the percentage of the intersection (area) with respect to the area of arene (Ph or subPh) ring.

X-ray powder diffraction data of the solids was collected using a PANalytical X'Pert PRO (HTK) diffractometer with Cu Kα radiation, acquired from 2Θ angles of 5° to 35° in steps of 0.034° at rt.

The crystallite size was determined using a crystallite size and strain analysis package included in Topas v2.1.

DSC analysis was performed in a Mettler Toledo DSC 1 instrument under an inert argon atmosphere. Samples (mass from 2 to 3 mg) were weighed in a light 20 μL Al pan. To prevent any evaporation of the sample, a pierced lid was pressed onto the sample using a special tool. For crystalline A and B samples, two heating and cooling cycles were performed under an inert flow of argon (flow 50 mL/min). The sample was heated from room temperature to 200 °C with a heating rate of 10 K/min, hold at final temperature for 5 min and then cooled again to room temperature at 10 K/min. This cycle was repeated once again. For studying crystallization behavior from amorphous materials, samples were heated under the same conditions. Prior to all measurements, the furnace was purged together with an inserted sample for 20 min to provide inert conditions. To estimate the sublimation temperature of crystalline solid B and additionally confirm that this sample sublimes before phase transformation and melting, a dynamic DSC measurement was performed in slightly different conditions, namely a larger hole with a diameter ∼1 mm was made in the lid to enable sample evaporation. The experiment was not performed in the open pan to avoid deposition of the sample in the DSC cell. The DSC analyzer was calibrated with high purity gallium and indium. Gallium was supplied by Physikalisch-Technische Bundesanstalt Braunschweig, whereas indium came from Mettler Toledo. DSC standards and all samples for DSC analysis were carefully weighed on a Mettler Toledo MX5 balance.

dx.doi.org/10.1021/ja501977a | J. Am. Chem. Soc. 2014, 136, 7383−7394

The solvents used in this work purchased from Fluka and Sigma-Aldrich were of spectrophotometric grade (≥ 99.7%) and used without further purification.

Absorption spectra were measured on a PerkinElmer Lambda 750 UV−vis spectrophotometer, and emission spectra on a PerkinElmer LS 55 spectrofluorometer with an excitation wavelength at 370 nm. Fluorescence spectra of solids were recorded with a front surface accessory from PerkinElmer and of single-crystals using a Well Plate Reader Accessory. The relative fluorescence quantum yields Φ_F in optically dilute solutions were estimated by standard methods[24] with quinine sulfate in 1 N H_2SO_4 as a reference (λ_{ex} = 347 nm; Φ_F = 0.508;[24c] n^{20} H_2O = 1.333) at rt.

The solid-state emission efficiencies relative to the pristine solid A were measured on prepared samples as follows: ∼1.5 mg of solid was added to a 200-fold excess of nonabsorbing KBr powder and gently homogenized in an agate mortar with a pestle to obtain an optically thick sample (3 mm). Then the emission spectrum of the sample was recorded over an integration range of 427−645 nm with an excitation wavelength at 370 nm.

The sample treated dropwise with dichloromethane was prepared in the following way: pristine solid sample (15 mg) was freshly ground in an agate mortar for at least 10 min to obtain the well ground solid. Then on adding a single drop of CH_2Cl_2 to the ground powder the yellow solid locally changes to the blue luminescent solid after about 1 min following evaporation of the solvent. The process of adding solvent drop by drop with intermediate evaporation repeated many times to achieve conversion of the entire ground powder to the blue-emitting crystalline solid A. The natural evaporation step in the process occurring between the each added drop of CH_2Cl_2 is very important to prevent the ground solid film becoming completely dissolved. The resulting crystalline solid was scraped from the mortar and examined by XRD measurement.

The morphological characteristics of the compounds obtained were investigated by SEM microscopy (field-emission FE-SEM Zeiss ULTRA PLUS) using an accelerating voltage of 2 kV. The samples were placed on graphite tape and were not gold sputtered prior to microscopy. Images were taken using a standard Evernhart-Thornley secondary electron (SE) detector.

Optical microscopy was conducted in the reflective light mode using a Zeiss Axio Imager microscope.

A Leica TCS SP5 laser scanning microscope mounted on a Leica DMI 6000 CS inverted microscope (Leica Microsystems, Germany) equipped with an 20× objective and excited with a blue laser (λ_{ex} = 405 nm) was used for CFM imaging. Fluorescence emission was detected in the range of 440−600 nm. For sequential excitation, a 50 mW 405 nm diode laser and the 476 nm line of a 25 mW argon laser were used.

4. CONCLUSIONS

The BF_2 complex of 1-phenyl-3-(3,5-dimethoxyphenyl)-propane-1,3-dione was shown to form two polymorphs, which are different in the mutual orientation of the two methoxy groups, resulting in changes in the modes of molecular packing. By controllable alteration of its molecular arrangements through external stimuli, varying solid-state emission was achieved from the same fluorophore. We observed that solid A but not solid B exhibited mechanochromic fluorescence and a striking CIEE effect; for instance, solid A emited strongly in the crystalline phase but only faintly in the amorphous phase (F_{max} = 490 and 526 nm, respectively), with a decrease in emission efficiency of as much as 5.3-fold. The yellow-emitting well ground powder of solid A on dropwise treatment with solvent (CH_2Cl_2) or on heating (thermochromism) reverted back to the initial blue-emissive crystal state, as well as partially returning to the original emission color spontaneously at room temperature (chronochromism). Additionally, solid A exhibited reversible switching emission on repeated grinding−heating processes, without displaying fatigue.

In contrast, after intensive grinding of the fluorescent yellow solid B in an agate mortar, followed by careful treatment with drops of CH_2Cl_2 or direct heating in a DSC instrument, the amorphous phase rearranged into the more stable crystalline phase A.

Further, heat-induced phase-to-phase interconversion between the two crystalline samples was found; thus, crystalline phase B converted to the thermodynamically more stable phase A at 162 °C, before melting, accompanied by a hypsochromic shift of 37 nm and a pronounced emission efficiency enhancement of 8.4-fold. Notably, the reinverse process is also accessible by complete dissolution of the resulting solid A in various solvents and subsequent evaporation.

Using additional methods such as SEM and CFM, we obtained supplementary evidence on the morphological changes during thermal treatment of the pristine solid B and a pure amorphous spin-cast film of **1**. Our findings can be summarized as follows. First the amorphous phase that exhibited a broad emission band remarkably red-shifted to 553 nm has a strong tendency for ordering. A small mechanical perturbation of the amorphous film formed some crystalline regions even before heating, while it crystallized promptly into crystalline phase A on thermal annealing. Next, making use of its appreciable vapor pressure the morphological structures and optical properties of the sublimate were revealed. Sublimation of the spin-cast amorphous film was performed in two different manners: slowly at 160 °C and rapidly at higher temperature to generate two types of microstructures, fluorescent platelike structures (emitting at 564 nm) or extremely thin crystalline microfibers (F_{max} = 555 nm) with lengths up to several hundreds of micrometers, respectively. In both cases the microstructures are constructed from segments in which the molecules self-organize by one-dimensional ordering, and show an obvious optical waveguide effect.

The absorption spectra of **1** are only slightly affected by the solvent polarity, whereas the center of its emission band alters from 431 nm in hexane (a nonpolar solvent) to 534 nm in polar CH_3CN with a huge decrease in fluorescence quantum yield. The alterations of the Stokes shift caused by various solvents elucidate the nature of the first electronically excited singlet state, which is more polarized than that in the ground state.

Dye **1** is also AIE active. Adding a large amount of water (f_w > 70 vol %) to the practically nonluminescent acetonitrile solution turns on its emission, being blue (crystalline phase A) or yellow (metastable amorphous solid, but which almost within a few minutes converts to a green suspension corresponding to phase B). The three distinct emission colors of **1** in suspensions with the same water content may be induced by diverse processes of aggregation. Fascinatingly, this is the first time that the way of addition of water, and not its content in the mixture, was utilized to fine-tune molecular packing during the aggregation process.

Finally, it is particularly important to understand the role of molecular packing in controlling the solid-state optical properties of dye **1** for developing stimuli-sensitive materials. We believe that this present work is worthy of attention not only in the field of fundamental research, but also in practical applications such as potential photoswitchable molecular devices, luminescent and sensory materials in optical displays,

dx.doi.org/10.1021/ja501977a | J. Am. Chem. Soc. 2014, 136, 7383−7394

chemical sensors, solid-state dye lasers, biomedical imaging, and others.

■ ASSOCIATED CONTENT

Supporting Information

XRD analyses, emission spectra, microscope images, theoretical calculation, crystallographic data (CIF), and detailed correlations of solvent spectral shifts. This material is available free of charge via the Internet at http://pubs.acs.org.

■ AUTHOR INFORMATION

Corresponding Author

boris.sket@fkkt.uni-lj.si

Notes

[†]A part of a Ph.D. dissertation.

The authors declare no competing financial interest.

■ ACKNOWLEDGMENTS

This work was supported by the Ministry of Higher Education, Science and Technology of the Republic of Slovenia and the Slovenian Research Agency (PR-4020). We are deeply grateful to Prof. Marjan Marinšek (Faculty of Chemistry and Chemical Technology, University of Ljubljana) for all photographs taken using SEM and optical microscopes, as well as for helpful discussion. We also thank Mojca Benčina, Ph.D. (National Institute of Chemistry, Ljubljana, Slovenia) for assistance in CFM measurements and the EN-FIST Centre of Excellence, Ljubljana, Slovenia for use of the SuperNova diffractometer.

■ REFERENCES

(1) (a) Cogné-Laage, E.; Allemand, J.-F.; Ruel, O.; Baudin, J.-B.; Croquette, V.; Blanchard-Desce, M.; Jullien, L. *Chem.—Eur. J.* **2004**, *10*, 1445−1455. (b) Hu, R.; Lager, E.; Aguilar-Aguilar, A.; Liu, J.; Lam, J. W. Y.; Sung, H. H. Y.; Williams, I. D.; Zhong, Y.; Wong, K. S.; Peña-Cabrera, E.; Tang, B. Z. *J. Phys. Chem. C* **2009**, *113*, 15845−15853. (c) Zhang, Z.; Bi, H.; Zhang, Y.; Yao, D.; Gao, H.; Fan, Y.; Zhang, H.; Wang, Y.; Wang, Y.; Chen, Z.; Ma, D. *Inorg. Chem.* **2009**, *48*, 7230−7236. (d) Zhang, G.; Lu, J.; Sabat, M.; Fraser, C. L. *J. Am. Chem. Soc.* **2010**, *132*, 2160−2162. (e) Jäkle, F. *Chem. Rev.* **2010**, *110*, 3985−4022. (f) Zhang, G.; Singer, J. P.; Kooi, S. E.; Evans, R. E.; Thomas, E. L.; Fraser, C. L. *J. Mater. Chem.* **2011**, *21*, 8295−8299. (g) Li, D.; Yuan, Y.; Bi, H.; Yao, D.; Zhao, X.; Tian, W.; Wang, Y.; Zhang, H. *Inorg. Chem.* **2011**, *50*, 4825−4831. (h) Rao, Y.-L.; Wang, S. *Inorg. Chem.* **2011**, *50*, 12263−12274. (i) Sun, X.; Zhang, X.; Li, X.; Liu, S.; Zhang, G. *J. Mater. Chem.* **2012**, *22*, 17332−17339. (j) Xu, S.; Evans, R. E.; Liu, T.; Zhang, G.; Demas, J. N.; Trindle, C. O.; Fraser, C. L. *Inorg. Chem.* **2013**, *52*, 3597−3610. (k) Zakrzewska, A.; Zaleśny, R.; Kolehmainen, E.; Ośmiałowski, B.; Jędrzejewska, B.; Ågren, H.; Pietrzak, M. *Dyes Pigm.* **2013**, *99*, 957−965.

(2) Shirai, K.; Matsuoka, M.; Fukunishi, K. *Dyes Pigm.* **1999**, *42*, 95−101.

(3) (a) Kubota, Y.; Tanaka, S.; Funabiki, K.; Matsui, M. *Org. Lett.* **2012**, *14*, 4682−4685. (b) Hong, Y.; Lam, J. W. Y.; Tang, B. Z. *Chem. Soc. Rev.* **2011**, *40*, 5361−5388.

(4) (a) Luo, J.; Xie, Z.; Lam, J. W. Y.; Cheng, L.; Chen, H.; Qiu, C.; Kwok, H. S.; Zhan, X.; Liu, Y.; Zhu, D.; Tang, B. Z. *Chem. Commun.* **2001**, 1740−1741. (b) Chen, J.; Law, C. C. W.; Lam, J. W. Y.; Dong, Y.; Lo, S. M. F.; Williams, I. D.; Zhu, D.; Tang, B. Z. *Chem. Mater.* **2003**, *15*, 1535−1546. (c) Tong, H.; Hong, Y.; Dong, Y.; Häussler, M.; Lam, J. W. Y.; Li, Z.; Guo, Z.; Guo, Z.; Tang, B. Z. *Chem. Commun.* **2006**, 3705−3707. (d) Zhao, Z.; Wang, Z.; Lu, P.; Chan, C. Y. K.; Liu, D.; Lam, J. W. Y.; Sung, H. H. Y.; Williams, I. D.; Ma, Y.; Tang, B. Z. *Angew. Chem., Int. Ed.* **2009**, *48*, 7608−7611. (e) Zhao, Z.; Chen, S.; Shen, X.; Mahtab, F.; Yu, Y.; Lu, P.; Lam, J. W. Y.; Kwok, H. S.; Tang, B. Z. *Chem. Commun.* **2010**, *46*, 686−688. (f) Yu, Z.; Duan, Y.; Cheng, L.; Han, Z.; Zheng, Z.; Zhou, H.; Wu, J.; Tian, Y. *J. Mater. Chem.* **2012**, *22*, 16927−16932.

(5) (a) Zhang, B. H.; Zhang, Z.; Ye, K.; Zhang, J.; Wang, Y. *Adv. Mater.* **2006**, *18*, 2369−2372. (b) Khlobystov, A. N.; Blake, A. J.; Champness, N. R.; Lemenovskii, D. A.; Majouga, A. G.; Zyk, N. V.; Schröder, M. *Coord. Chem. Rev.* **2001**, *222*, 155−192. (c) Varghese, S.; Das, S. *J. Phys. Chem. Lett.* **2011**, *2*, 863−873.

(6) (a) Dong, Y.; Lam, J. W. Y.; Qin, A.; Li, Z.; Sun, J.; Sung, H. H.-Y.; Williams, I. D.; Tang, B. Z. *Chem. Commun.* **2007**, 40−42. (b) Tong, H.; Dong, Y.; Hong, Y.; Häussler, M.; Lam, J. W. Y.; Sung, H. H.-Y.; Yu, X.; Sun, J.; Williams, I. D.; Kwok, H. S.; Tang, B. Z. *J. Phys. Chem. C* **2007**, *111*, 2287−2294.

(7) (a) Tong, H.; Dong, Y.; Häussler, M.; Lam, J. W. Y.; Sung, H. H.-Y.; Williams, I. D.; Sun, J.; Tang, B. Z. *Chem. Commun.* **2006**, 1133−1135. (b) Li, H.; Chi, Z.; Zhang, X.; Xu, B.; Liu, S.; Zhang, Y.; Xu, J. *Chem. Commun.* **2011**, *47*, 11273−11275.

(8) (a) Hong, Y.; Lam, J. W. Y.; Tang, B. Z. *Chem. Commun.* **2009**, 4332−4353. (b) Wang, M.; Zhang, G.; Zhang, D.; Zhu, D.; Tang, B. Z. *J. Mater. Chem.* **2010**, *20*, 1858−1867.

(9) (a) Que, E. L.; Domaille, D. W.; Chang, C. J. *Chem. Rev.* **2008**, *108*, 1517−1549. (b) Gonçalves, M. S. T. *Chem. Rev.* **2009**, *109*, 190−212. (c) Klymchenko, A. S.; Mely, Y. *Prog. Mol. Biol. Transl.* **2013**, *113*, 35−58.

(10) (a) Zhao, B. Y.; Gao, H.; Fan, Y.; Zhou, T.; Su, Z.; Liu, Y.; Wang, Y. *Adv. Mater.* **2009**, *21*, 3165−3169. (b) Luo, X.; Li, J.; Li, C.; Heng, L.; Dong, Y. Q.; Liu, Z.; Bo, Z.; Tang, B. Z. *Adv. Mater.* **2011**, *23*, 3261−3265. (c) Abe, Y.; Karasawa, S.; Koga, N. *Chem.—Eur. J.* **2012**, *18*, 15038−15048. (d) Harada, N.; Abe, Y.; Karasawa, S.; Koga, N. *Org. Lett.* **2012**, *14*, 6282−6285.

(11) (a) Bouas-Laurent, H.; Dürr, H. *Pure Appl. Chem.* **2001**, *73*, 639−665. (b) Beyer, M. K.; Clausen-Schaumann, H. *Chem. Rev.* **2005**, *105*, 2921−2948. (c) Mizuguchi, J.; Tanifuji, N.; Kobayashi, K. *J. Phys. Chem. B* **2003**, *107*, 12635−12638. (d) Sagara, Y.; Mutai, T.; Yoshikawa, I.; Araki, K. *J. Am. Chem. Soc.* **2007**, *129*, 1520−1521. (e) Ito, H.; Saito, T.; Oshima, N.; Kitamura, N.; Ishizaka, S.; Hinatsu, Y.; Wakeshima, M.; Kato, M.; Tsuge, K.; Sawamura, M. *J. Am. Chem. Soc.* **2008**, *130*, 10044−10045. (f) Perruchas, S.; Goff, X. F. L.; Maron, S.; Maurin, I.; Guillen, F.; Garcia, A.; Gacoin, T.; Boilot, J.-P. *J. Am. Chem. Soc.* **2010**, *132*, 10967−10969.

(12) Krishna, G. R.; Kiran, M. S. R. N.; Fraser, C. L.; Ramamurty, U.; Reddy, C. M. *Adv. Funct. Mater.* **2013**, *23*, 1422−1430.

(13) Zhang, X.; Zhang, G. *Anal. Methods* **2012**, *4*, 2641−2643.

(14) (a) Liu, T.; Chien, A. D.; Lu, J.; Zhang, G.; Fraser, C. L. *J. Mater. Chem.* **2011**, *21*, 8401−8408. (b) Nguyen, N. D.; Zhang, G.; Lu, J.; Sherman, A. E.; Fraser, C. L. *J. Mater. Chem.* **2011**, *21*, 8409−8415.

(15) (a) Tang, C. W.; VanSlyke, S. A. *Appl. Phys. Lett.* **1987**, *51*, 913. (b) Burroughes, J. H.; Bradley, D. D. C.; Brown, A. R.; Marks, R. N.; Mackay, K.; Friend, R. H.; Burns, P. L.; Holmes, A. B. *Nature* **1990**, *347*, 539−541. (c) Chen, H. Y.; Lam, W. Y.; Luo, J. D.; Ho, Y. L.; Tang, B. Z.; Zhu, D. B.; Wong, M.; Kwok, H. S. *Appl. Phys. Lett.* **2002**, *81*, 574. (d) Lam, J. W. Y.; Tang, B. Z. *Acc. Chem. Res.* **2005**, *38*, 745−754.

(16) (a) Parab, K.; Venkatasubbaiah, K.; Jäkle, F. *J. Am. Chem. Soc.* **2006**, *128*, 12879−12885. (b) Qin, Y.; Kiburu, I.; Shah, S.; Jäkle, F. *Macromolecules* **2006**, *39*, 9041−9048. (c) Nagai, A.; Kokado, K.; Nagata, Y.; Chujo, Y. *Macromolecules* **2008**, *41*, 8295−8298. (d) Nagata, Y.; Otaka, H.; Chujo, Y. *Macromolecules* **2008**, *41*, 737−740. (e) Zhou, Y.; Xiao, Y.; Chi, S.; Qian, X. *Org. Lett.* **2008**, *10*, 633−636. (f) Zhang, G.; St. Clair, T. L.; Fraser, C. L. *Macromolecules* **2009**, *42*, 3092−3097.

(17) Kononevich, Y. N.; Meshkov, I. B.; Voronina, N. V.; Surin, N. M.; Sazhnikov, V. A.; Safonov, A. A.; Bagaturyants, A. A.; Alfimov, M. V.; Muzafarov, A. M. *Heteroat. Chem.* **2013**, *24*, 271−282.

(18) Galer, P.; Košmrlj, B.; Šket, B. *Tetrahedron* **2011**, *67*, 2103−2109.

(19) Mirochnik, A. G.; Fedorenko, E. V.; Kuryavyi, V. G.; Bukvetskii, B. V.; Karasev, V. E. *J. Fluoresc.* **2006**, *16*, 279−286.

(20) Wang, J.; Mei, J.; Hu, R.; Sun, J. Z.; Qin, A.; Tang, B. Z. *J. Am. Chem. Soc.* **2012**, *134*, 9956−9966.

(21) (a) Reichardt, C.; Welton, T. *Solvents and Solvent Effects in Organic Chemistry*; Wiley-VCH: Weinheim, Germany, 2011. (b) Nigam, S.; Rutan, S. *Appl. Spectrosc.* **2001**, *55*, 362A−370A.
(22) Manohara, S. R.; Kumar, V. U.; Shivakumaraiah; Gerward, L. *J. Mol. Liq.* **2013**, *181*, 97−104.
(23) Kirillova, A. Y. *Russ. J. Gen. Chem.* **2007**, *77*, 1463−1464.
(24) (a) Demas, J. N.; Crosby, G. A. *J. Phys. Chem.* **1971**, *75*, 991−1024. (b) Fery-Forgues, S.; Lavabre, D. *J. Chem. Educ.* **1999**, *76*, 1260−1264. (c) Velapoldi, R. A.; Tønnesen, H. H. *J. Fluoresc.* **2004**, *14*, 465−472.